Universal active metasurfaces for ultimate wavefront molding by manipulating the reflection singularities

Mahmoud Elsawy, Christina Kyrou, Elena Mikheeva, Rémi Colom, Jean-yves Duboz, Khosro Zangeneh Kamali, Stéphane Lanteri, Dragomir Neshev, Patrice Genevet

Abstract Optical metasurfaces are becoming ubiquitous optical components to mold the amplitude, phase, and polarization of light. So far, most of these devices are passive in essence, that is, they cannot be arbitrarily reconfigured or optimized according to the user's interest and/or change in the surrounding environment. Here we propose an innovative design strategy relying on the position of topological singularities, namely zeros and poles of the reflection coefficient, to address full phase modulation of light reflected off an active metasurface with almost unity efficiency. The active metasurface unit cells, consisting of asymmetric Gires-Tournois resonators filled with either silicon or hetero-structured materials to leverage on the thermo-optical or electro-optical effects, respectively. In both cases, a full phase modulation associated with 100% reflection amplitude is observed even when dealing with extremely low refractive index change, on the order of $\Delta n \approx 0.01$. Improving the deflection efficiencies for each deflection angle and accounting for the near-field coupling between strongly resonant pixels is performed by calculating the refractive index modulation profile in the extended unit cell using an advanced optimization methodology relying on statistical learning. Consequently, active beam steering designs for active thermo-optical effect with ultimate performance exceeding 90% have been optimized. Furthermore, active wavefront splitting using electro-optics materials was optimized to reach ultimate modulation performances with nearly 92% efficiency. The realization of highly efficient active beam-forming operating at high frequencies would open important applications in imaging microscopy, high-resolution image projection, optical communication, and 3D light detection and ranging (LiDAR).

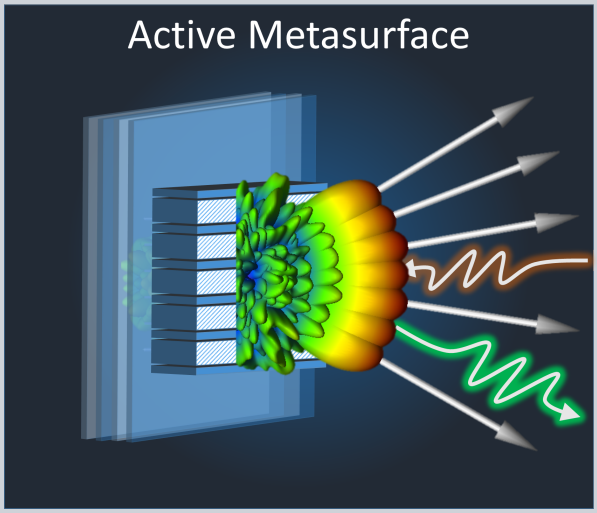

GUIDE

Universal active metasurfaces for ultimate wavefront molding by manipulating the reflection singularities

Mahmoud M. R. Elsawy[1,*], Christina Kyrou[2], Elena Mikheeva[2], Rémi Colom[2], Jean-Yves Duboz[2], Khosro Zangeneh Kamali[3], Stéphane Lanteri[1], Dragomir Neshev[3], and Patrice Genevet[2,*]

1. Introduction

Metasurfaces (MSs) are functional optical interfaces composed of subwavelength assemblies of optically thin nanostructured elements [1–4]. The interest in MSs has kept growing continuously for more than a decade, driven by their compatibility with planar semiconductor fabrication technology and their potential for integration into optoelectronic devices. In this context, ultra-compact metasurface-based deflectors, beam splitters, lenses, waveplates, and holograms are approaching unitary wavefront-molding efficiencies [5–10]. Currently three methods are used to efficiently address the local phase, amplitude, or polarization of light. The first method uses the modification of the effective refractive index (ERI) of low-quality factor truncated nano-waveguides [3,6,11,12]. The second method leverages the Pancharatnam Berry (PB) phase imprinted by birefringent particles on the polarization-converted light [13–16]. Finally, the third phase addressing mechanism relies on the resonant scattering of light and the associated light scattering modulation properties, using plasmonic or dielectric scatterers [17–20]. While the first two methods are presumably well-understood, recent works addressing the last phase modulation method revealed an intriguing connec-

[1] Université Côte d'Azur, Inria, CNRS, LJAD, 06902 Sophia Antipolis Cedex, France
[2] Université Côte d'Azur, CNRS, CRHEA, Sophia Antipolis, Valbonne, France
[3] TMOS, Research School of Physics, The Australian National University, Canberra, ACT 2601, Australia

[*] Corresponding author: e-mail: mahmoud.elsawy@inria.fr; e-mail: patrice.genevet@crhea.cnrs.fr

tion between the full phase modulation and the topological effects governing the light interaction with resonant nanoparticles [21]. Extending these tuning mechanisms to the active regime would offer real-time and ultra-fast wavefront modulation [22]. Tunable MS are triggering real enthusiasm in the community, driven mainly by their low-cost scalable manufacturing capabilities for large volume applications in active beam steering for Light Detection and Ranging (LiDAR) [23–25], AR/VR wearable devices, varifocal lenses [26, 27] and so forth [28]. They are expected to provide extreme wavefront molding versatility, opening up a broad scope of applications. When tuning the MS, it is of paramount importance to actively correct for the impact of fabrication imperfections and near-field coupling between nanostructures. Such correction can drastically improve device performances, especially for devices operating in a non-local regime, however, it has not been demonstrated to date.

To realize active MS, two distinct approaches have been considered so far. The first relies on addressing the pixel-by-pixel dynamical material response to adapt the device's optical properties via distributed external stimuli [29, 30]. The second approach relies on mechanical, electrical, and chemical actuation to directly tune the whole MS [27, 31, 32, 32–34]. This second approach, however, cannot provide arbitrary wavefront reconfigurability. We, therefore, focus on the first approach, as we are searching for an ideal pixel-by-pixel tunable meta-MS with high efficiency. Maximizing the transmission or reflection across the entire modulation range is not a straightforward task when operating at the nanoscale. Key challenges include poor electromagnetic field confinement, the difficulty in independently addressing each element, and the extremely weak modulation effect caused by the short interaction distance (typically on the order of a μm-thick). To circumvent these problems, choosing the right combination between material and phase tuning mechanisms is necessary. Dynamic light modulation at metasurfaces has been proposed using various material platforms, including Phase Change Materials (PCMs) [35–38], Liquid Crystals (LC) [28], thermo-optic (TO) [39] or electro-optic (EO) effects [40]. PCMs offer large refractive index modulation ($\Delta n \sim 1$) but exhibit significant losses in the VIS and NIR wavelength range. LCs benefit from high industrial maturity and large Δn (in the range of $0.1 - 0.3$, however, they have relatively slow ($\lesssim$kHz) modulation speed. The TO effect could reach similar index modulation with faster speed, however, it could result in the overall heating of the sample, as it mainly relies on passive cooling. The EO effect exhibits fast modulation speed ($>$ 1GHz) however is accompanied by a tiny refractive index change, usually on the order of $\Delta n \sim 10^{-3}$. Because each of these mechanisms has a different refractive index modulation Δn, a different resonant configuration is required to achieve full 2π phase modulation.

The modulation speed is also a concern when dealing with active tuning. As the modulation speed increases, the material's Δn generally decreases. Therefore, achieving both fast and large phase tuning becomes particularly challenging. Here, we address this issue by employing optical metasurfaces of high-quality factor (high-Q) resonances. However, a full 2π phase modulation in such metasurfaces is generally accompanied with undesirable amplitude changes, which need to be mitigated. To better understand the optical modulation properties of high-Q resonant structures, we propose to analyze their responses in the complex frequency plane, and in particular by examining the position of their topological singularities, namely the resonances and the associated zeros of the reflection coefficient. We show how to manipulate and exploit the positions of singularities in the complex plane to achieve phase only modulation with almost unity amplitude. We exemplify this concept by theoretically studying a reflective Gires-Tournois (G-T) cavity [41]. We then exploit our theoretical findings to design highly efficient G-T active metasurfaces comprising either the thermo-optical effect in Si nanoridges or the quantum confined Stark effect in multiple quantum wells hetero-structured materials. Furthermore, a global optimization technique is employed to maximize the beam-forming response by accounting for non-local response and near-field coupling between neighboring structures [42, 43]. Our work highlights the role played by topological singularities in the scattering response of nanostructures and proves that optimization methods are becoming mandatory to modulate light efficiently, in particular when dealing with devices operating in the strong non-local coupling regime.

2. Understanding and exploiting the reflection singularities of Gires-Tournois nanoresonators

Reasonably assuming that Fabry-Pérot (F-P), G-T, and metasurfaces are exchanging energy with their environment, they can similarly be considered as open linear physical systems that are well represented by a matrix connecting input and output fields through a linear response function. We explore the reflection coefficient of a theoretical F-P cavity in the complex frequency plane to theoretically investigate these devices in the presence of radiation losses. In this complex plane, the imaginary part of the frequency represents the absorption or scattering losses [44]. Our analysis is based on the study of the complex-valued zeros and poles of the reflection coefficient, which are topological phase singularities. The positions of these singularities greatly influence the phase and the amplitude of the reflection coefficient on the real axis. More precisely, our objective is to identify the parameter condition for which zeros and poles are separated by the real axis in the complex frequency plane. This configuration yields a 2π phase accumulation along the real frequency axis [21]. We then study the influence of the zero-pole relative position with respect to the real axis on the quality factor of the resonance.

It is relatively trivial to write the analytical expression for the reflection coefficient of an F-P cavity consisting of a lossless medium of refractive index n and thickness t, enclosed between two mirrors with different real value reflection coefficients, defined as r_2 for the lower and r_1 for the upper mirror, respectively [41]. Considering an input

field E_{in} (we choose the sign convention as $e^{-i\omega t}$) normally incident on the cavity (Fig. 1(a)), one can express the overall device's reflection coefficient r of the F-P cavity as [45]:

$$r = E_r/E_{in} = (r_1 + r_2 e^{i\delta})/(1 + r_1 r_2 e^{i\delta}) \quad (1)$$

where δ denotes the phase accumulation in the cavity given by $\delta = 2\omega nt/c$. Here, ω is the operating frequency in vacuum, c is the speed of light, and E_r is the reflected electromagnetic field. This quantity can be expanded on complex-valued poles and zeros using the Weierstrass factorization theorem [46–51], where each factor depends on the frequencies of the singularities, i.e., poles $\omega_{p,m}$ and zeros $\omega_{z,m}$. Based on our sign convention choice $e^{-i\omega t}$, zeros could have both positive or negative imaginary parts depending on the parameter condition, while pole always have a negative imaginary part to satisfy causality. Hence, the Weierstrass factorizatio yields:

$$r(\omega) = \prod_m \frac{\omega - \omega_{z,m}}{\omega - \omega_{p,m}} \quad (2)$$

where

$$\omega_{z,m} = (2m-1)\frac{c\pi}{nt} - i\frac{c}{2nt}\log(r_1) + i\frac{c}{2nt}\log(r_2)$$

and

$$\omega_{p,m} = (2m-1)\frac{c\pi}{nt} + i\frac{c}{2nt}\log(r_1) + i\frac{c}{2nt}\log(r_2).$$

Here m is an integer representing the cavity round-trip resonances. As r_1 and r_2 are real-valued and smaller than one, $\log(r_1)$ and $\log(r_2)$ are negative.

Eq. (1) defines the position of the poles and zeros in a complex plane as a function of the reflectivity of the lower and upper mirrors. Thus, this expression completely determines the amplitude and the phase of the cavity response [52]. Let us consider only the case of a G-T cavity, i.e., we assume a constant reflectivity of the lower mirror $r_2 = 1$ and keep a refractive index $n = 1.5$ and a thickness $t = 600\ nm$ for the rest of the theoretical derivation (see Fig. 1(a) for more details). This choice implies that a G-T cavity has only one incoming and one outgoing/reflecting channel. In this case, the scattering matrix reduces to a single coefficient which is the reflection coefficient [53]. For a lossless system, the time-reversal symmetry is preserved so that the scattering poles and zeros are complex conjugates, i.e., $\omega_p = \omega_z^*$ (see Eq. (2) and Ref. [50, 51]). This is theoretically confirmed by setting $r_2 \to 1$ in the expressions for $\omega_{\mathrm{z,m}}$ and $\omega_{\mathrm{p,m}}$, leading to complex conjugate zeros and poles for $r(\omega)$. Assuming ω to be complex in Eq. (1) and plotting the reflection amplitude and phase in the complex frequency plane, we indeed observe two connected complex frequency singularities, as depicted in Figs.1 (b) and (c).

When the condition $\omega_p = \omega_z^*$ is fulfilled, the reflection coefficient features unity reflection amplitude and full 2π phase modulation when the real frequency varies from 0 to infinity (in fact in a smaller frequency range as will be detailed later, in Fig.1 (e)) as predicted analytically and shown in Figs.1 (b) and (c).

Once r_2 is set to unity, the upper mirror reflectivity r_1 is used to control the quality factor of the resonance. Using the expression for $\omega_{\mathrm{z,m}}$ and $\omega_{\mathrm{p,m}}$, we theoretically predict the position and trajectories of the zero and pole singularities (zero-pole pairs) as a function of r_1, as shown in Fig.1(d).Increasing r_1, i.e., creating a cavity with a higher quality factor, decreases the absolute value of the imaginary parts of both singularities, corresponding to decreased losses. The losses vanish at the limit $r_1 = 1$, and the system becomes Hermitian with real eigenvalues. Considering the necessity of 2π phase modulation, we plot in Fig. 1(d) the relative position of zeros and poles as a function of r_1, i.e., as a function of the Q-factor of the cavity. It shows that the distance in the imaginary plane of a zero-pole pair of singularities decreases by increasing the quality factor. In Fig. 1(e), we present the evolution of the phase as a function of the real frequency with varying r_1. It shows that the phase modulation sharpens as a function of the frequency for increasing quality factor, thus correlating the phase modulation range with the imaginary value of the complex singularities. From our analysis of the G-T reflection in the complex frequency plane, the conditions for achieving full phase modulation and the unity efficiency are: zero-pole singularities have to be complex conjugated and their imaginary part has to be sufficiently small, that is, zero-pole have to be sufficiently close to each other, to experience rapid phase modulation as a function of the frequency.

Fig. 1(f) illustrates the analogy made between a G-T resonator and an asymmetric metasurface resonator. The first design step consists in controlling the metasurface reflectivity to operate as a top G-T mirror through the excitation of a low/high-quality resonance. We considered a single GaN resonator ($n = 2.38$) embedded in a vacuum and designed the structure to position the first magnetic dipole mode around $\lambda = 550$ nm. To mimic the G-T configuration, the resonator is then placed on top of a distributed Bragg reflector (DBR) composed of HfO_2/SiO_2 as shown in Fig. 1(f).

The reflection amplitude and phase maps as functions of the wavelength and the number of DBR pairs are presented in Fig. 1(g). When the reflectivity of the lower mirror increases (with an increasing number of DBR pairs), the presence of a reflection zero on the real axis is observed at approximately 9 DBR pairs (line 3 in Fig. 1(g)), i.e., exactly when a phase singularity appears in the corresponding phase map panel. As for the GT-cavity, this behavior might be better understood by studying the positions of reflections zeros and poles in the complex plane. The locations of the complex-valued reflection zeros and poles are shown in Fig. 1(h). They were determined by performing numerical computations using the finite-element method based solver JCMsuite [54]. For a small reflectance of the lower mirror, both the zero (blue dot) and the pole (red dot) are located below the real axis, i.e., both have negative imaginary parts. The corresponding phase does not vary much over the wavelength range displayed in Fig. 1(g), right plot. As the number of DBR pairs increases, the positions of zeros and poles move upwards. For a given number of DBR pairs (9 in this example), the zero reflection amplitude reaches the

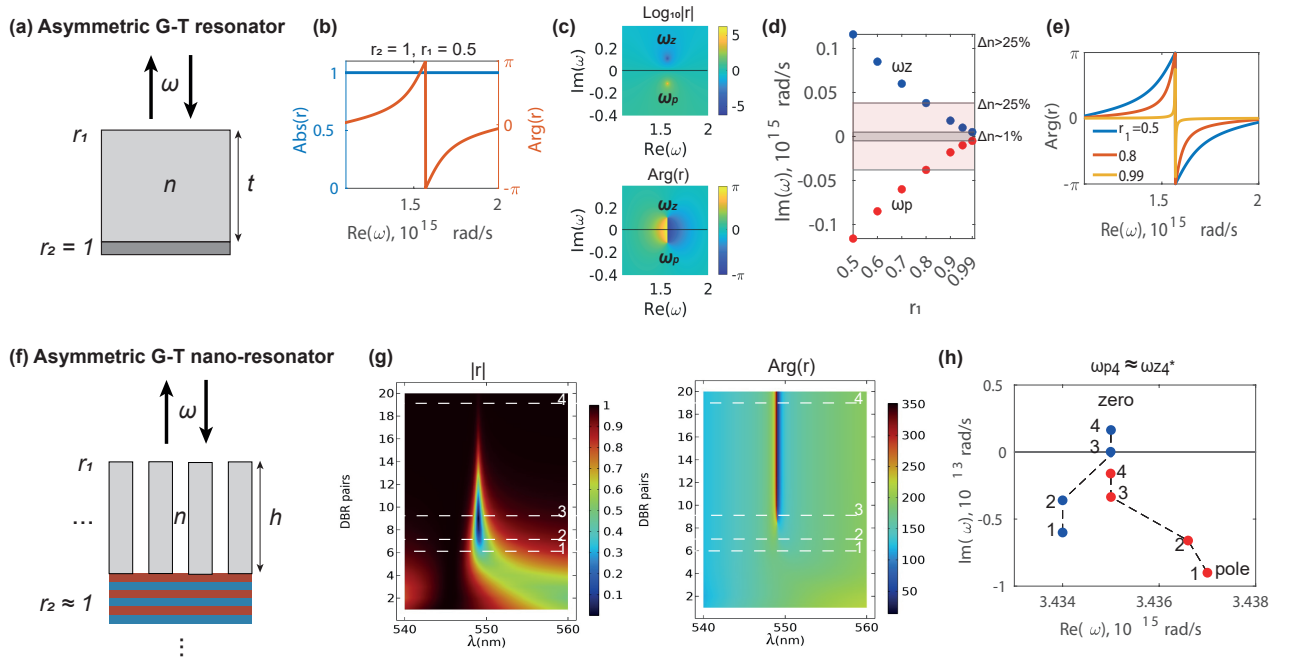

Figure 1 Theoretical description of a non-Hermitian G-T linear system and its analogy with a reflecting metasurface configuration. (a) Schematic representation of a G-T resonator consisting of a layer of thickness t and refractive index n surrounded by two mirrors with reflection coefficients r_1 and r_2. (b) Reflection amplitude and phase produced by the G-T cavity in (a) with $n = 1.5$, $t = 600\ nm$, $r_2 = 1$, $r_1 = 0.5$. (c) The amplitude and phase of the reflection coefficient, given the complex frequency in Eq. (1), where the line $Im(\omega) = 0$ corresponds to the result in (b). (d) Positions of the complex poles and zeros for a fixed reflectivity of the bottom mirror $r_2 = 1$ when the reflectivity of the top mirror r_1 is varied. As r_1 approaches unity, the zero-pole pairs approach the real axis, which increases the resonance quality factor. We identify the regions of the zero-pole pairs corresponding to different relative refractive index changes to achieve full 2π phase modulation in the tuning. (e) The reflection phase corresponds to the result in (d) for different values of r_1. (f) Schematic configuration of 2D GaN nanoridge (in grey) disposed in air and on the top of a distributed Bragg Reflecting (DBR) mirror composed of HfO_2 ($n = 1.9$) and SiO_2 ($n = 1.47$) thin film pairs, as indicated by the blue and red layers, respectively. (g) Color plot indicating reflection amplitude and the reflection phase evolution for light impinging at normal incidence as a function of the excitation frequency and the number of the DBR pairs. We observe the presence of a zero of reflection in the spectrum (i.e., at real frequencies) for about 9 DBR pairs, i.e., exactly when a phase singularity appears in the associated phase map. We indicate with numbered lines the number of DBR pair values for which the complex position of poles and zeros are numerically calculated and shown in (h). In panel (h), complex-valued reflection zeros and poles are shown as blue and red dots, respectively. For 6 and 7 DBR pairs, both the zeros and poles lie below the real axis. For 9 DBR pairs, the reflection zero reaches the real axis, as was already observed in panel (g). For 19 pairs, the zero moves to the upper part of the complex plane, separating the zero and pole on either side of the real axis, thus reaching the condition for full 2π-phase modulation, as confirmed in phase map in panel g). Also, increasing the number of DBR pairs approaches r_2 closer to 1, thus reaching the G-T characterized by $\omega_p = \omega_z^*$ and corresponding to unity reflection amplitude. For all figures (f,g,h), the parameters of the GaN ridge are fixed with a width of 180 nm, a height of 200 nm, and $n_{GaN} = 2.38$.

real axis around the resonance wavelength ($\lambda = 550$ nm). This situation reflects to the condition of critical coupling, corresponding to point 3 in Fig. 1(h), and becomes a Reflectionless Scattering Mode (RSM) [53, 55]. This intersection of the reflection zero with the real axis corresponds to the zero region identified in Fig. 1(g).

Increasing further the number of DBR pairs, the zero moves into the upper part of the complex plane, while the pole remains confined under the real axis to satisfy the principle of causality. This condition leads to the appearance of the sharp 2π phase jump, see Fig. 1(g). The sufficient condition for a 2π phase accumulation related to the existence of the zero-pole pair separated by the real axis explains the phase behavior observed in Fig. 1(g) for a number of DBR pairs larger than 9. Further increasing the bottom reflectivity yields a progressive increase of the reflection amplitude until the system reaches constant unity reflection. This corresponds, as expected, to the condition where zero and pole become complex conjugated of one another, see blue and red dots denoted 4 in Fig. 1(h).

Note that full phase modulation for a similar geometry has been reported by tuning the geometrical parameters of a dielectric resonator on top of a highly reflective substrate [45]. 0 to 2π full phase addressing has been obtained using conventional real frequency excitation simulations [45]. Here we approach the problem from the complex

frequency analysis, giving deeper insights and a rigorous physical explanation of the modulation properties. In the following, we will further exploit these results to conceive an active metasurface wavefront modulator, which is adjusted pixel-by-pixel to demonstrate high-performance active beam steering and deflection.

3. Electrically tunable Gires-Tournois Metasurfaces

3.1. Thermo-optical tuning of the light with reflective resonant cavities

In this section, we propose an active MS modulation scheme that follows the recommendation derived in Sec. 2. It takes into consideration the physical requirements underlying the phase and unity amplitude modulation of the cavity resonance, i.e., a unity reflectivity for the lower interface and a relatively sufficient high-Q resonance such that full phase modulation can be experienced using the thermo-optical effect in silicon (Si) nano-ridges. We are concerned about experimental implementation and propose a simple design that can solve the fabrication challenges in tunable reflective G-T metasurfaces with ultimate performance. Silicon exhibits a relatively large thermo-optical effect, $\Delta n = \frac{dn}{dT}\Delta T$, that can be utilized to alter the metasurface scattering properties. Here, $\frac{dn}{dT}$ is the material thermo-optic coefficient. Previously, the thermo-optical effect of amorphous silicon has been exploited to introduce a sizable change in the refractive index of $\Delta n = 0.21$ by increasing its temperature from room temperature to 300°C [39, 56]. Aside from its large thermo-optic coefficient, the silicon's electrical properties allow it to be used as a resistive heater [57,58]. Here we use a ridge-metasurface design (Fig. 2(a)), where each ridge serves as a localized resistive heater by applying a voltage across their end cross-sections. The generated heat in each ridge (and, therefore, its temperature) can be controlled by varying the current fed through the ridges.

Following the procedure in Sec. 2, we first consider a unit cell where a Si ridge is completely surrounded by SiO_2 and excited from the top with an x-polarized light, propagating in the z-direction. Fig. 2(a) is a 3D schematic of the unit cell, invariant in the y-direction. The width W and thickness H are optimized to achieve high modal confinement in the Si region for the designed wavelength of $\lambda = 1500$ nm. A sharp resonant response is realized in the reflection spectrum, as shown in Figs. 2(b-c). The unit-cell period in Fig. 2(b) has been set as $P = 600$ nm, while the width W and the thickness H are fixed at 280 nm and 810 nm, respectively. The refractive index of Si at low temperatures is fixed at 3.48. After identifying the standalone resonant properties of the nano-ridge array, we place the unit-resonator on the top of a reflective gold layer (of thickness 200 nm). To achieve G-T reflectivity conditions and avoid light trapping in the gold layer, we vary the distance D (Fig. 2(d)) between the Si nano-ridge and the gold layer. As shown in Fig. 2(e-f), as the distance D increases, the reflection amplitude increases to near unity, associated with a 2π phase modulation. In other words, the reflection zero converges to the condition of complex conjugation with its pole. Fig. 2(g) finally shows the response of an active G-T unit cell with fixed geometric parameters and modulating the Si refractive index between 0 and 0.25. As seen, one achieves unitary reflection as well as over a 2π phase variation.

Further assembling a periodic arrangement of several of these ideal unit-cells presented in Fig. 2(d), we design an efficient thermally programmable beam steering device. The results presented in Fig. 3(a-c) and (d-f) correspond to periodic electrical activation of six and four pixels, respectively, by applying a programmable pixel-by-pixel temperature control. In Fig. 3(a), each Si pixel is subjected to an individual potential difference, resulting in a different refractive index modulation. Due to the sub-wavelength pixel size, the reflected beam will be directed to the first diffraction order, according to the generalized law of reflection [1]. The main objective is then to maximize the light directed in the $+1$ lobe, that is, to find the Δn value for each Si ridge to steer the normally incident light in the desired direction with unity efficiency. Optimization can also be used to account for the strong near-field coupling between unit cells induced by the resonances. It is important to note that independent of the specific modulation technique, the overall performances of the fabricated metasurfaces remained relatively low, with wavefront addressing efficiency often below 70% , even for devices operating near their optimal design condition. The MS building blocks can be finely tuned to take near-field coupling between adjacent elements and local changes in the MS surrounding environment into account. These effects are particularly noticeable in MS operating in the nonlocal regime, with strongly resonant nano-cells [59–64]. The accurate choice of the refractive index distribution among the repeated unit pixels is realized here by relying on an advanced optimization method known as efficient global optimization (EGO), specifically targeting the design of the metasurfaces [5, 42, 43, 65]. In EGO, a surrogate model is used to statistically select the best candidates for the next simulation of the system. The optimization results (for the 6-pixel case) are depicted in Fig. 3(b). The refractive index values required for efficient beam-steering have been optimized after only 100 iterations, illustrating the potential of EGO for fast optimization of metasurface's performances.

The illustrations in Fig. 3(a) and (d) present the variation of the refractive index, as it is intuitively expected to design a blazed grating. The numerical optimization, however, yields a non-linear and even a non-monotonous variation of the refractive index along the pixels, as shown in Tab. 1 and the corresponding phase map, given in Fig. 2(g). This is due to strong near-field coupling between pixels. As illustrated in Fig. 3(c), the optimal parameters (voltage distribution or extraordinary refractive index modulation) yield a maximum of reflected power directed to the $+1$ order with an efficiency exceeding 93% with a 36° Field of View (FoV). A similar optimization has been performed for periodic arrangements of four pixels, leading to 75% beam steering efficiency in the $+1$ order in Fig. 3(f) with a higher steering angle of 50° FoV, as illustrated in Fig. 3(d-f). The optimiza-

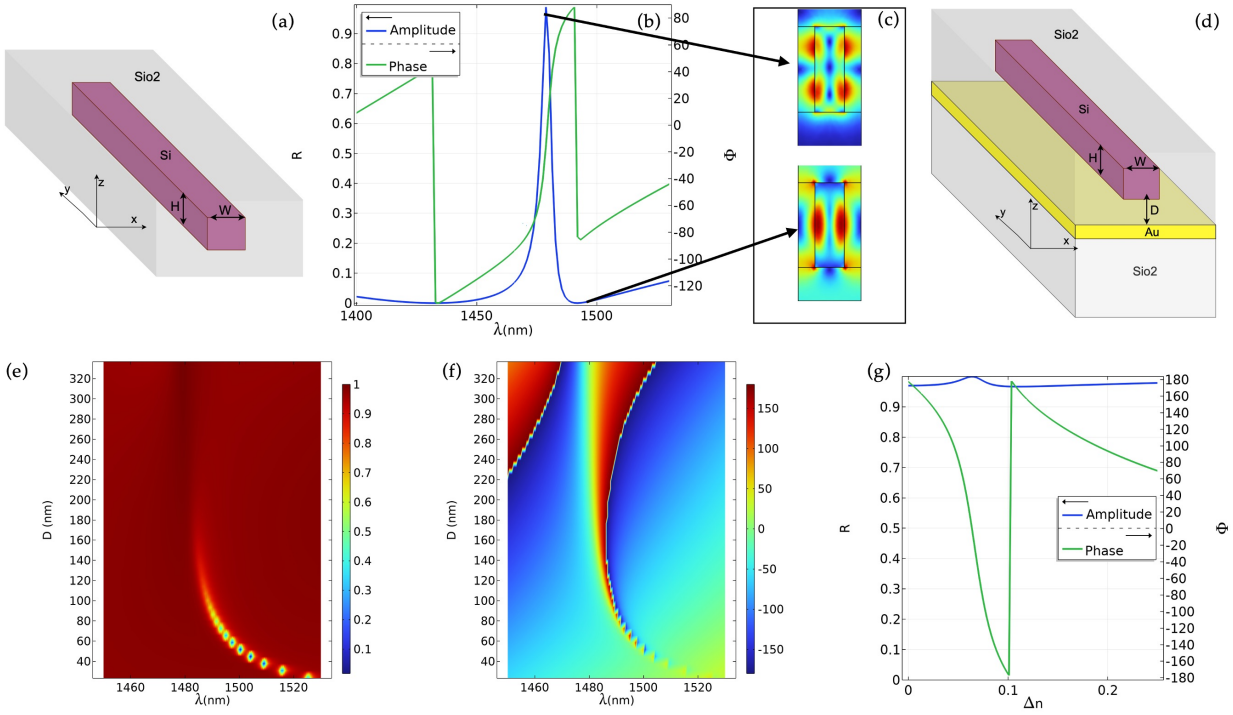

Figure 2 Schematic representation of an ideal active metasurface unit-cell based on thermo-optical effect to actively tune the reflected phase. (a-c) refer to a Si unit-cell resonator surrounded by SiO_2, that is without a reflecting substrate and excited by a normally incident x-polarized light impinging from the top, whereas (d-g) represents the same resonator disposed on a thin gold layer of thickness 200 nm. The excitation also consists of an x-polarized beam coming at normal incidence. (a) A homogeneous Sio_2 encapsulates a Si nano-ridge with dimensions of $H = 810$ nm and width $W = 280$ nm. The period of the unit cell is fixed at 600 nm, and the width and the thickness have been optimized to observe a sharp feature in the reflection spectrum around the desired wavelength of $\lambda = 1500$ nm, as shown in (b). The corresponding cross-section of the electric field distribution (along the $x-z$ plane) is shown in (c). (d) To take advantage of the G-T phase modulation mechanism discussed earlier, the resonator is placed on a thin reflective gold layer (thickness 200 nm) separated from the Si nano-ridge by a distance D. The reflection response amplitude and phase maps as a function of the distance D and the wavelength λ are depicted in (e-f). Increasing the value of D results in nearly 100% of the reflection amplitude with a $2pi$ phase response, in agreement with the expected ideal G-T functionality discussed in Sec. 2. (f) depicts the reflected amplitude and phase modulation as a function of refractive index change. The latter is considered to be tuned via an external thermal stimulus with a maximum of $\Delta n = 0.25$ at the operation wavelength $\lambda = 1500$ nm.

Modulation	6 pixels	4 pixels
Δn_1	0.1188	0
Δn_2	0.1621	0.08133
Δn_3	0.250	0.150
Δn_4	0.0068	0.25
Δn_5	0.020	-
Δn_6	0.0541	-

Table 1 Optimized values of the Si refractive index modulation (Δn) in each unit cell to diffract light on the first order only with maximal efficiency. The second and third columns correspond to the active metasurface unit cells composed of 6 and 4 pixels as depicted in Fig. 3(a) and (d), respectively.

tion results after 100 iterations for this second case are given in Fig. 3(e). As indicated in the second column of Tab. 1, non-trivial refractive index distribution is required to mitigate the near-field coupling between pixels. To the best of our knowledge, this is the highest performance obtained so far for an active beam steering device using a simple configuration in reflection [66].

3.2. Towards GHz beam steering using the electro-optic effect in a quantum-confined Stark light modulator

Tunable metasurfaces exploiting electro-optical effects have been proposed for dynamic wavefront engineering delivering exceptionally high modulation frequencies, up to the GHz range [40]. In this section, we propose an ultra-fast dynamic wavefront shaping metasurface operating in reflection using an electro-optic III–V MQW modulator [64]. The optical response of the MQW, particularly the refractive index, can be continuously tuned by applying an external voltage. Confined electron and hole levels in the QW are shifted

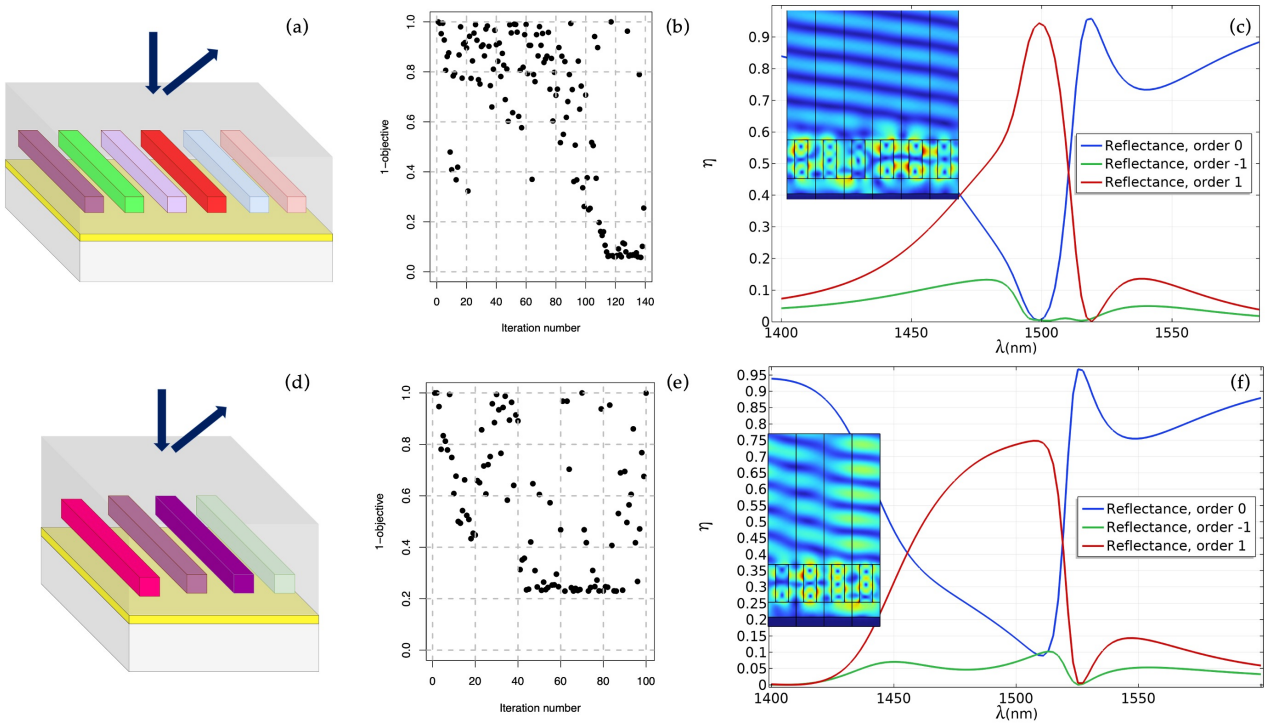

Figure 3 Active beam steering using an array of active G-T Si nanoresonators. Periodic electrical activation of six (a) and four (d) unit cells with pixel-by-pixel refractive index modulation. The optimization results for each case are depicted in (b) and (e), respectively. The beam steering responses after the optimized refractive index distribution in the sequential pixels are shown in panels (c) and (f) for six- and four- pixels configuration, respectively, with the corresponding field map at the design wavelength $\lambda = 1500$ nm. The optimization parameters represent the refractive index distribution in each pixel represented by different colors in (a) and (d). The corresponding refractive index values are given in Tab. 1.

in energy by the electric field via the so-called Quantum Confined Stark Effect (QCSE) [67, 68]. The associated shift of the absorption edge leads to a change in the refractive index, which is maximum for photon energies near the absorption band edge. With QCSE, the modulation frequency is theoretically limited by the dielectric relaxation rate and practically limited by RC terms that have to be minimized in the design and fabrication. Modulation frequencies up to the GHz frequency range can be envisioned. As mentioned previously, increasing the modulation speed reduces the refractive index modulation. For QCSE modulation, the latter is generally within the 2%, which was previously the bottleneck for achieving highly efficient design [67, 68]. To minimize losses, one has to operate at photon energy below the absorption edge but not too far below to keep a large index modulation. Moreover, experimental observation of GHz modulation speed would require minimizing the parasitic RC constants as the latter certainly exceeds the intrinsic dielectric relaxation rate.

Recently, Ref. [64] reported on an active metasurface based on electro-optically tunable AlGaAs/GaAs MQW supporting hybrid Mie-guided mode resonance at $\lambda = 915$‘nm. In their work, the MQW yields a maximum refractive index modulation of $\Delta n = 0.01$. A specific unit cell with high-quality Mie-guided mode resonance was considered to achieve a maximum phase modulation of 70 degrees with 30% reflection amplitude in the vicinity of the refractive index modulation of $\Delta n = 0.01$. Accordingly, an active beam splitter with modest power and overall efficiency of less than 10% is realized at $\lambda = 915$ nm. Very recently, a numerical work realizing high-performance active metasurfaces by exploiting the linear electro-optic effect in Lithium Niobate ($LiNbO_3$) with a $\Delta n \approx 0.07$ index modulation has been proposed [69]. The structure consists of elongated nano-bars composed of Silicon (Si) on $LiNbO_3$, placed between two planar Indium-tin-Oxide (ITO) electrodes. High-Q guided mode resonances (GMR) leading to full 2π phase modulation are realized by adding sub-wavelength periodic notches parallel to the nanobar periodicity. In this section, we consider an MQW heterostructure similar to the one used in Ref. [64], i.e., with a refractive index modulation of $\Delta n = 0.01$, and report on efficient sub-wavelength pixels featuring performances comparable with the latest state-of-the-art.

The proposed sub-wavelength pixel is shown in Fig. 4(a), where an active MQW region is encapsulated between two horizontal conductive electrodes. As previously discussed, high-Q metasurface elements are designed to exhibit significant optical modulation across a refractive index modulation of $\Delta n = 0.01$. Similar to Sec. 3.1, we consider a

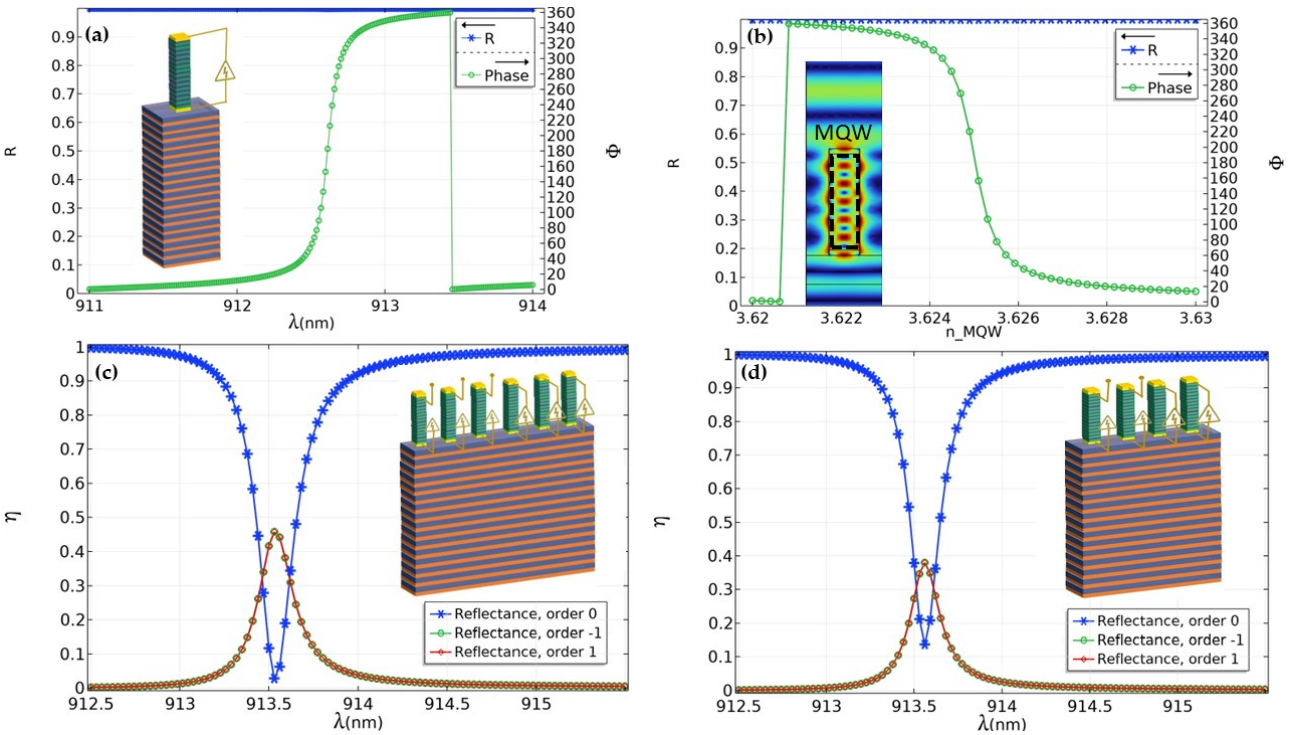

Figure 4 Ultra-fast programmable beam splitting relying on quantum-confined Stark modulation in an MQW heterostructure (green and purple layers correspond to GaAs and AlGaAs, respectively). (a) The reflection phase and amplitude for the optimized sub-wavelength pixel are depicted in the inset. The active MQW region is encapsulated between two conductive electrodes (here, we have considered p-doped GaAs). The resonator is placed on a DBR made of SiO_2/HfO_2 pairs (blue/orange sequences) on top of HfO_2 substrate. The geometrical parameters are as follows: $P = 450$ nm, width $w = 180$ nm, thickness $H = 910$ nm. Besides, the thicknesses of the two electrodes are fixed as 50 nm with a refractive index of 3.55, and the effective refractive index of the MQW is chosen as in Ref. [64] as 3.62. The response of the single unit cell without the DBR is presented in Fig. 7 in the supplementary information section. (b) Efficient metasurface response at $\lambda = 913.5$ nm upon the application of the external voltage across the MQW (the inset refers to the electric field distribution into the resonator for $v = 0$). (c-d) Programmable active beam splitting with 6 (c) and 4 (d) pixels designed to deflect light at an angle of 40, and $= 60$ degrees, respectively. The refractive index distribution is given in the supplementary information section 8.

single unit cell surrounded by vacuum and tune the thickness H and the width W to produce a high-quality resonant mode confined in the MQW region (the amplitude and phase response together with the field profiles are given in Fig. 7(a-b) in the supplementary information). The presence of top and bottom contact electrodes introduces impedance mismatch responsible for Fabry-Perot resonance inside the pillar. A uniform reflection amplitude and full phase accumulation as a function of the incident wavelength within a narrow wavelength range, as described in Sec. 2, is again obtained by adding a reflective lower DBR mirror consisting of SiO_2/HfO_2 pairs (see Fig. 4(a)). The evolution of the phase and amplitude as a function of the reflectivity of the lower mirror (DBR pairs) is presented in the supplementary information (see Fig. S7(d)), where the G-T condition is observed for over 12 DBR pairs. Achieving 2π-phase accumulation in such a small wavelength range is needed to address a large phase variation as a function of the refractive index modulation for a fixed design wavelength, as demonstrated in Fig. 4(b).

We have exploited the ideal sub-wavelength pixels numerically to design high-efficiency programmable beam splitters. We considered programmable beam splitter designs with binary voltage to alter the deflection angle (in ± 1 orders) as a function of period and applied voltages, as shown in Fig. 4(c-d). The expected overall efficiency reaches 90% and 80% with a FOV of 40° and 60°, respectively. It is worth noting that the binary phase distribution produced by the optimization is counter-intuitive (see Supplementary Fig. S8) but still provides the highest beam splitting power at the desired wavelength by accounting for strong near-field coupling. This ultimate performance, based on a realistic configuration and considering simple geometric features with a refractive index modulation of $\Delta n \sim 0.01$, demonstrates our design's potential for ultrafast beam steering.

4. Conclusion

In conclusion, we propose a simple methodology to design active metasurfaces operating in reflection. We studied the complex frequency response of a generic Fabry-Perot resonator, namely the position of zeros and poles of the reflection coefficient in the complex frequency plane. Using this approach, we have identified the conditions required to design an efficient tunable cavity. We conclude that *i*) unity reflection requires a conjugated pair of zero-pole singularities and *ii*) their imaginary part has to be chosen accordingly to the modulation depth, that is zero and pole have to be sufficiently close to each other such that the reflection experience a full phase modulation, as a function of the material modulation depth. We implement these conditions to demonstrate that light reflecting from a G-T resonator may undergo a strong resonant full non-linear 2π phase modulation with near unity reflection. The resonant phase can be modified by varying the cavity thickness, the operation frequency, or the refractive index of interest, thus leading to active phase tuning. Classical phase gradient designs, relying on conventional look-up-tables, are not necessarily leading to efficient beam forming. We observed that the strong resonant character of the excited optical modes magnifies further the near-field coupling effect between the resonators. We rely on a global optimization strategy to tackle this problem and demonstrate a considerable improvement in the MS beam-steering efficiency at each deflection angle. Two realistic designs consisting of semiconductor G-T cavities exploiting either thermo-optical effects in Si nano-cells or electro-optical effect in multiple quantum wells structures have been considered to demonstrate active deflection and beam steering at extreme field-of-view with ultimate performance exceeding 90%

The design of active metasurfaces relying on materials presenting non-isotropic material response, generally characterized by a dielectric tensor, for example one could consider liquid crystals, requires additional care. Indeed, the resonant nature of the GT mode considered herein provides both transverse and longitudinal field distributions, along x- or y- depending on the input polarization but also along the z-direction oriented along the propagation. The optimization of the deflector operating with such anisotropic materials offers new and interesting perspectives of research and applications beyond the content of this manuscript. Our results also open up new and realistic perspectives for the conception of tunable metasurfaces with unexpected high frequency and high amplitude modulation capabilities for LiDARs and reconfigurable wavelength-division multiplexers in optical networks.

Acknowledgments

RC, EM, and PG acknowledge Dr. Sven Burger and JCMwave for their help and support with the JCMsuite software. KZK and DN acknowledge useful discussions with Prof. Mohsen Rahmani and Dr. Lei Xu.

Funding

SL, ME, and PG acknowledge support from the French defense procurement agency under the ANR ASTRID Maturation program, grant-agreement number ANR-18-ASMA-0006-01. RC acknowledges support from the European Innovation Council (EIC) project TwistedNano (under the grant agreement number Pathfinder Open 2021- 101046424). PG and EM acknowledge financial support from the French National Research Agency ANR Project Meta-On-Demand (ANR-20-CE24-0013). CK has been supported with a postdoctoral fellowship grant by the Bodossaki Foundation (Athens, Greece). KZK and DN acknowledge the support of the Australian Research Council, Centres of Excellence program (CE20010001).

Key words: Tunable metasurfaces, Gires-Tournois asymmetric cavity, Thermo-Optical, Quantum-Confined Stark Effect, LiDAR

References

[1] N. Yu, P. Genevet, M. A. Kats, F. Aieta, J. P. Tetienne, F. Capasso, and Z. Gaburro, science **334**(6054), 333–337 (2011).
[2] P. Genevet, F. Capasso, F. Aieta, M. Khorasaninejad, and R. Devlin, Optica **4**(1), 139–152 (2017).
[3] S. Astilean, P. Lalanne, P. Chavel, E. Cambril, and H. Launois, Optics letters **23**(7), 552–554 (1998).
[4] D. Lin, P. Fan, E. Hasman, and M. L. Brongersma, Science **345**(6194), 298–302 (2014).
[5] M. M. Elsawy, A. Gourdin, M. Binois, R. Duvigneau, D. Felbacq, S. Khadir, P. Genevet, and S. Lanteri, ACS photonics **8**(8), 2498–2508 (2021).
[6] S. Wang, P. C. Wu, V. C. Su, Y. C. Lai, M. K. Chen, H. Y. Kuo, B. H. Chen, Y. H. Chen, T. T. Huang, J. H. Wang et al., Nature nanotechnology **13**(3), 227–232 (2018).
[7] W. T. Chen, A. Y. Zhu, V. Sanjeev, M. Khorasaninejad, Z. Shi, E. Lee, and F. Capasso, Nature nanotechnology **13**(3), 220–226 (2018).
[8] M. Pan, Y. Fu, M. Zheng, H. Chen, Y. Zang, H. Duan, Q. Li, M. Qiu, and Y. Hu, Light: Science & Applications **11**(1), 1–32 (2022).
[9] Q. Song, A. Baroni, R. Sawant, P. Ni, V. Brandli, S. Chenot, S. Vézian, B. Damilano, P. de Mierry, S. Khadir et al., Nature communications **11**(1), 1–8 (2020).
[10] Y. Y. Xie, P. N. Ni, Q. H. Wang, Q. Kan, G. Briere, P. P. Chen, Z. Z. Zhao, A. Delga, H. R. Ren, H. D. Chen et al., Nature nanotechnology **15**(2), 125–130 (2020).
[11] P. Lalanne, S. Astilean, P. Chavel, E. Cambril, and H. Launois, JOSA A **16**(5), 1143–1156 (1999).
[12] M. Khorasaninejad and F. Capasso, Nano letters **15**(10), 6709–6715 (2015).
[13] Z. Bomzon, G. Biener, V. Kleiner, and E. Hasman, Optics letters **27**(13), 1141–1143 (2002).
[14] M. Khorasaninejad and K. B. Crozier, Nature communications **5**(1), 1–6 (2014).
[15] M. Khorasaninejad, W. T. Chen, R. C. Devlin, J. Oh, A. Y. Zhu, and F. Capasso, Science **352**(6290), 1190–1194 (2016).
[16] Y. Tian, X. Jing, H. Yu, H. Gan, C. Li, and Z. Hong, Optics Express **28**(21), 32107–32123 (2020).

[17] W. Liu and Y. S. Kivshar, Optics express **26**(10), 13085–13105 (2018).
[18] Y. F. Yu, A. Y. Zhu, R. Paniagua-Domínguez, Y. H. Fu, B. Luk'yanchuk, and A. I. Kuznetsov, Laser & Photonics Reviews **9**(4), 412–418 (2015).
[19] L. Huang, X. Chen, H. Mühlenbernd, H. Zhang, S. Chen, B. Bai, Q. Tan, G. Jin, K. W. Cheah, C. W. Qiu et al., Nature communications **4**(1), 1–8 (2013).
[20] M. S. Bin-Alam, O. Reshef, Y. Mamchur, M. Z. Alam, G. Carlow, J. Upham, B. T. Sullivan, J. M. Ménard, M. J. Huttunen, R. W. Boyd et al., Nature communications **12**(1), 1–8 (2021).
[21] R. Colom, E. Mikheeva, K. Achouri, J. Zuniga-Perez, N. Bonod, O. J. Martin, S. Burger, and P. Genevet, arXiv preprint arXiv:2202.05632 (2022).
[22] E. Mikheeva, C. Kyrou, F. Bentata, S. Khadir, S. Cueff, and P. Genevet, ACS Photonics **9**(5), 1458–1482 (2022).
[23] J. Park, B. G. Jeong, S. I. Kim, D. Lee, J. Kim, C. Shin, C. B. Lee, T. Otsuka, J. Kyoung, S. Kim et al., Nature nanotechnology **16**(1), 69–76 (2021).
[24] I. Kim, R. J. Martins, J. Jang, T. Badloe, S. Khadir, H. Y. Jung, H. Kim, J. Kim, P. Genevet, and J. Rho, Nature nanotechnology **16**(5), 508–524 (2021).
[25] R. Juliano Martins, E. Marinov, M. Youssef, C. Kyrou, M. Joubert, C. Colmagro, V. Gâté, C. Turbil, P. M. Coulon, D. Turover et al., Nature communications **13**(1), 1–8 (2022).
[26] C. Y. Fan, T. J. Chuang, K. H. Wu, and G. D. J. Su, Optics Express **28**(7), 10609–10617 (2020).
[27] E. Arbabi, A. Arbabi, S. M. Kamali, Y. Horie, M. Faraji-Dana, and A. Faraon, Nature communications **9**(1), 1–9 (2018).
[28] S. Q. Li, X. Xu, R. Maruthiyodan Veetil, V. Valuckas, R. Paniagua-Domínguez, and A. I. Kuznetsov, Science **364**(6445), 1087–1090 (2019).
[29] H. Weigand, V. V. Vogler-Neuling, M. R. Escalé, D. Pohl, F. U. Richter, A. Karvounis, F. Timpu, and R. Grange, ACS Photonics **8**(10), 3004–3009 (2021).
[30] J. Sautter, I. Staude, M. Decker, E. Rusak, D. N. Neshev, I. Brener, and Y. S. Kivshar, ACS nano **9**(4), 4308–4315 (2015).
[31] R. Kaissner, J. Li, W. Lu, X. Li, F. Neubrech, J. Wang, and N. Liu, Science Advances **7**(19), eabd9450 (2021).
[32] C. Meng, P. C. Thrane, F. Ding, J. Gjessing, M. Thomaschewski, C. Wu, C. Dirdal, and S. I. Bozhevolnyi, Science Advances **7**(26), eabg5639 (2021).
[33] C. A. Dirdal, P. C. Thrane, F. T. Dullo, J. Gjessing, A. Summanwar, and J. Tschudi, Optics Letters **47**(5), 1049–1052 (2022).
[34] Q. He, S. Sun, and L. Zhou, Research **2019** (2019).
[35] S. Cueff, J. John, Z. Zhang, J. Parra, J. Sun, R. Orobtchouk, S. Ramanathan, and P. Sanchis, APL Photonics **5**(11), 110901 (2020).
[36] Y. Zhang, C. Fowler, J. Liang, B. Azhar, M. Y. Shalaginov, S. Deckoff-Jones, S. An, J. B. Chou, C. M. Roberts, V. Liberman et al., Nature Nanotechnology **16**(6), 661–666 (2021).
[37] S. Lepeshov and A. Krasnok, Nature Nanotechnology **16**(6), 615–616 (2021).
[38] S. Cueff, A. Taute, A. Bourgade, J. Lumeau, S. Monfray, Q. Song, P. Genevet, B. Devif, X. Letartre, and L. Berguiga, Advanced Optical Materials **9**(2), 2001291 (2021).
[39] M. Rahmani, L. Xu, A. E. Miroshnichenko, A. Komar, R. Camacho-Morales, H. Chen, Y. Zárate, S. Kruk, G. Zhang, D. N. Neshev, and Y. S. Kivshar, Advanced Functional Materials **27**(31), 1700580 (2017).
[40] I. C. Benea-Chelmus, S. Mason, M. L. Meretska, D. L. Elder, D. Kazakov, A. Shams-Ansari, L. R. Dalton, and F. Capasso, Nature Communications **13**(1), 1–9 (2022).
[41] F. Gires and P. Tournois, Comptes Rendus Hebdomadaires Des Seances De L Academie Des Sciences **258**(25), 6112 (1964).
[42] M. M. Elsawy, M. Binois, R. Duvigneau, S. Lanteri, and P. Genevet, Optics Express **29**(19), 29887–29898 (2021).
[43] M. M. Elsawy, S. Lanteri, R. Duvigneau, G. Brière, M. S. Mohamed, and P. Genevet, Scientific reports **9**(1), 1–15 (2019).
[44] H. M. Nussenzveig, Causality and dispersion relations, Tech. rep., 1972.
[45] S. Colburn, A. Zhan, and A. Majumdar, scientific Reports **7**(1), 1–9 (2017).
[46] M. C. Hutley and D. Maystre, Optics Communications **19**(3), 431–436 (1976).
[47] R. A. Depine, V. L. Brudny, and J. M. Simon, Optics Letters **12**(3), 143–145 (1987), Publisher: Optica Publishing Group.
[48] L. C. Botten, M. Cadilhac, G. H. Derrick, D. Maystre, R. C. McPhedran, M. Neviere, and P. Vincent, Electromagnetic Theory of Gratings, softcover reprint of the original 1st ed. 1980 edition edition (Springer, Berlin, Heidelberg, December 2011).
[49] D. Maystre, Theory of Wood's Anomalies, in: Plasmonics, edited by S. Enoch and N. Bonod (Springer Berlin Heidelberg, Berlin, Heidelberg, 2012), pp. 39–83.
[50] V. Grigoriev, S. Varault, G. Boudarham, B. Stout, J. Wenger, and N. Bonod, Physical Review A **88**(6), 063805 (2013).
[51] A. Krasnok, D. Baranov, H. Li, M. A. Miri, F. Monticone, and A. Alú, Advances in Optics and Photonics **11**(4), 892 (2019).
[52] E. A. Bezus, D. A. Bykov, and L. L. Doskolovich, Opt. Lett. **45**(18), 5065–5068 (2020).
[53] W. R. Sweeney, C. W. Hsu, and A. D. Stone, Physical Review A **102**(6), 063511 (2020), Publisher: American Physical Society.
[54] J. Pomplun, S. Burger, L. Zschiedrich, and F. Schmidt, physica status solidi (b) **244**(10), 3419–3434 (2007).
[55] W. Yang, S. Sun, C. Zhang, J. Li, Z. Duan, Q. Song, and S. Xiao, Scientific Reports **6**(1), 1–6 (2016).
[56] K. Zangeneh Kamali, L. Xu, J. Ward, K. Wang, G. Li, A. E. Miroshnichenko, D. Neshev, and M. Rahmani, Small **15**(15), 1805142 (2019).
[57] M. Jacques, A. Samani, E. El-Fiky, D. Patel, Z. Xing, and D. V. Plant, Opt. Express **27**(8), 10456–10471 (2019).
[58] S. De, R. Das, R. K. Varshney, and T. Schneider, IEEE Access **8**, 141632–141640 (2020).
[59] H. Cai, S. Srinivasan, D. A. Czaplewski, A. B. Martinson, D. J. Gosztola, L. Stan, T. Loeffler, S. K. Sankaranarayanan, and D. López, npj Computational Materials **6**(1), 1–8 (2020).
[60] C. Gigli, Q. Li, P. Chavel, G. Leo, M. L. Brongersma, and P. Lalanne, Laser & Photonics Reviews **15**(8), 2000448 (2021).
[61] S. C. Malek, A. C. Overvig, A. Alù, and N. Yu, arXiv preprint arXiv:2009.07054 (2020).

[62] A. C. Overvig, S. C. Malek, and N. Yu, Physical Review Letters **125**(1), 017402 (2020).

[63] J. Park, B. G. Jeong, S. I. Kim, D. Lee, J. Kim, C. Shin, C. B. Lee, T. Otsuka, J. Kyoung, S. Kim et al., Nature nanotechnology **16**(1), 69–76 (2021).

[64] P. C. Wu, R. A. Pala, G. Kafaie Shirmanesh, W. H. Cheng, R. Sokhoyan, M. Grajower, M. Z. Alam, D. Lee, and H. A. Atwater, Nature communications **10**(1), 1–9 (2019).

[65] M. M. Elsawy, S. Lanteri, R. Duvigneau, J. A. Fan, and P. Genevet, Laser & Photonics Reviews **14**(10), 1900445 (2020).

[66] P. Thureja, R. Sokhoyan, C. U. Hail, J. Sisler, M. Foley, M. Y. Grajower, and H. A. Atwater, Nanophotonics **11**(17), 3745–3768 (2022).

[67] J. Lee, S. Jung, P. Y. Chen, F. Lu, F. Demmerle, G. Boehm, M. C. Amann, A. Alù, and M. A. Belkin, Advanced Optical Materials **2**(11), 1057–1063 (2014).

[68] Y. H. Kuo, Y. K. Lee, Y. Ge, S. Ren, J. E. Roth, T. I. Kamins, D. A. Miller, and J. S. Harris, Nature **437**(7063), 1334–1336 (2005).

[69] E. Klopfer, S. Dagli, D. Barton III, M. Lawrence, and J. A. Dionne, Nano Letters **22**(4), 1703–1709 (2022).

[70] S. Lanteri, C. Scheid, and J. Viquerat, SIAM J. Sci. Comp. **39**(3), 831–859 (2017).

[71] Diogenes: A Discontinuous-Galerkin based software suite for nano-optics, https://diogenes.inria.fr/.

[72] O. Roustant, D. Ginsbourger, and Y. Deville, Journal of Statistical Software **51**(1), 1–55 (2012).

Mahmoud M. R. Elsawy received his PhD from the University of Aix-Marseille, France, in 2017, specializing in optics, photonics, and image processing. The topic of his PhD thesis was dedicated to the development of computational models for the design of realistic integrated nonlinear plasmonic waveguides. He spent a year as a postdoctoral researcher at the Institut Fresnel in Marseille, France. After a postdoc at Inria Sophia Antipolis, France, in the field of numerical optimization of nanophotonics, he became a permanent member of the Atlantis project team in December 2020 as an Inria Starting Faculty Position (ISFP). His research activities focus on the modeling and design of innovative passive and programmable metasurface devices.

Christina Kyrou Christina Kyrou received her PhD from the National and Kapodistrian University of Athens, Greece, in 2019. Her PhD research has been devoted to the investigation of the impact of nanoparticles on the liquid-crystalline order. In 2020, C. Kyrou was awarded with individual funding from the Bodossaki Foundation (Greece) for her project "Active Plasmonic Devices." In 2022, she was selected as the laureate of the i-PhD contest of innovation supported by BPi France and the french government for her project "AUTONOM" dealing with tunable metasurfaces for LiDAR applications. Since 2020 she is a postdoctoral researcher in P. Genevet's group, working on the conceptualization and demonstration of programmable metasurfaces.

Elena Mikheeva Elena Mikheeva received her Ph.D. degree in 2020 from the University of Aix-Marseille that followed a joint European Master program EUROPHOTONICS in Aix-Marseille University and Karlsruhe Institute of Technology (2015-2017). While completing these studies, Elena worked on the design, fabrication, and characterization of optical components, mainly focusing on wavefront-shaping metasurfaces. In 2021 Elena joined the group of P. Genevet as a postdoctoral fellow working on the fundamental aspects of metasurfaces design, including tunable devices.

Rémi Colom holds a joint PhD from Aix-Marseille University and the University of Sydney. He is currently working as a post-doctoral researcher at CNRS-CRHEA, Valbonne, France. He previously worked as a postdoctoral researcher at the Zuse Institute Berlin and as a temporary lecturer at Avignon University.

Jean Yves Duboz Jean-Yves Duboz specializes in electronic and optical properties of semiconductors and related heterostructures, in particular III-V semiconductors. His field of expertise also includes the physics of devices, in particular optoelectronic devices. After his PhD at CNET-Grenoble working on Si-silicide heterostructures, he worked at IBM-T.J.Watson, Yorktown Heights (USA) on InGaAs/InAlAs HEMTs. Then he joined the Research Lab of Thales in Orsay (France), studying intersubband transitions and developing quantum wells, infrared detectors, optical modulators, and UV detectors based on AlGaN. He spent one year at the National Research Council of Canada in Ottawa, working on quantum dot detectors and diluted nitrides. In 2002 he joined CNRS-CRHEA in Valbonne, France. He developed GaN-based lasers, nanophotonic devices, extreme UV, X-ray, and proton detectors. He owns 11 patents and more than 140 publications. H factor 30 (google scholar).

Khosro Zangeneh Kamali is a PhD student at the Australian National University under the ARC Centre of Excellence for TMOS. His research activities focus on designing, fabricating, and characterizing thermally tunable metasurfaces.

Stéphane Lanteri received a PhD degree in engineering sciences at the University of Nice Sophia Antipolis, France, in 1991. After a postdoc in the Aerospace Engineering Department of the University of Colorado at Boulder, he was appointed as a junior research scientist at Inria Sophia Antipolis, France in November 1993. He is currently a senior research Scientist at Inria and the head of a project-team whose research activities aim at the design and study of innovative mathematical methods for the numerical modeling of nanoscale light-matter interactions. His research interests are concerned with high order finite element methods (Discontinuous Galerkin methods) and high-performance multiscale solvers for the numerical treatment of full-wave differential models of nanophotonics. He also coordinates the development of the DIOGENeS software suite (https://diogenes.inria.fr/) dedicated to computational nanophotonics, which was initiated in December 2015

Dragomir Neshev is a Professor of Physics at the Australian National University (ANU) and the Director of the Australian Research Council Centre of Excellence for Transformative Meta-Optical Systems (TMOS). He received a PhD degree from Sofia University, Bulgaria, in 1999. Since then, he has worked in the field of optics at several research centres around the world and joined ANU in 2002. He is the recipient of several awards and honors, including a Highly Cited Researcher (Web of Science, 2021), a Queen Elizabeth II Fellowship (ARC, 2010), and a Marie-Curie Individual Fellowship (European Commission, 2001). His activities span several branches of optics, including periodic photonic structures, singular optics, plasmonics, and optical metasurfaces.

Patrice Genevet received his Ph. D. degree at the université Côte d'Azur, France in 2009 on localized spatial solitons in semiconductor lasers and amplifiers. He did five years as a research fellow (2009-2014) in the Capasso group (SEAS, Harvard University) in collaboration with Prof. M.O. Scully (Texas A & M University). In 2014, he obtained the position of senior research scientist at A*STAR, Singapore. In 2015, He joined CNRS as 'Chargé de Recherche'. He is the recipient of the 2017 Aimé-Cotton Price from the French Physical Society, the ERC Starting Grant 2015 on "Functional flat optical components and applications," the 2019 ERC proof of Concept, and the 2021 Fabry-De Gramont Price from the French Optical Society. P. Genevet research activities concern the development of optical metamaterials, passive and active metasurfaces, and their applications and integration in optoelectronic devices. He owns 6 patents and 97 publications. H factor 46 (Google Scholar)

Supplementary information

Numerical methods

Full-wave electromagnetic solver

The full-wave electromagnetic simulations for the active tunable metasurface presented in this paper were generally performed using our in-house high-order full-wave electromagnetic solver based on the Discontinuous Galerkin method (DG) [70]. This full-wave solver is implemented in the DIOGENeS [71] software suite programmed in Fortran 2008 and adapted to high-performance computer systems. For comparison, we also performed full-wave simulations based on the finite element approach (FEM) using COMSOL Multiphysics® v. 6.0. In Fig. 5 we show the excellent agreement between the two solvers in the case of the thermal modulation configuration with 4 pixels presenting various refractive index modulations, as shown in Fig. 3(f). The opto-geometric parameters can be found in the caption of Fig. 3(f) and tab. 1 (third column).

Statistical learning optimization

In our work, we relied on an advanced optimization method based on statistical learning using the `R` packages `DiceKriging` [72]. This method is known as EGO. It is based on a surrogate modeling that replaces the high-fidelity process of electromagnetic evaluation with a simpler and cheaper model for predicting the new designs during the optimization process. Although it converges to a global solution set, it requires fewer iterations than the classical global evolutionary strategies in the single-objective and multi-objective optimization configurations, as we have previously shown [5, 42, 43].

Complex analysis calculations

The complex analysis calculations presented in Fig. 1 and 6 to compute pole-zero positions in the complex plane are computed analytically by solving Eq. 1. The results presented in Fig. 1(h) are computed from the JCMsuite software for the structure given in 1(f).

GT complex frequency analytical description

The analytical results from Eq. 1 describing a G-T cavity filled with glass $n = 1.5$ of thickness $t = 600$ *nm* provides clear and intuitive description of the response of a reflective metasurface. Modifying the bottom mirror reflectivity r_2 while keeping r_1 fixed at 0.5, it is possible to control reflected efficiency and presence of the 2π resonant phase jump as illustrated by Fig.6(b),(c). These phase and amplitude maps can be divided in different regions: (i) when $r_2 < r_1$, both pole and zero are located in the lower part of the complex plane. As such, the branch cut connecting zero and pole of the reflection coefficient does not cross the real axis. Therefore, no 2π jump is produced in reflection for real frequency excitation as confirmed in Fig.6d). (ii) When $r_1 = r_2$, the system is in the condition of critical coupling [53] which means that the reflection zero is located on the real axis. It results in reflection amplitude reaching zero at real frequency excitation and reflection zero experiencing a π jump, as evidenced in Fig.6e). (iii) In the situation when $r_2 > r_1$, the branch cut starts crossing the real axis producing a desired 2π phase jump. However, the proximity of the zero to the real frequency axis results in a low reflection efficiency, see Fig.6f) . (iv) describe the optimal design condition satisfied when $r_2 = 1$. For the latter case, the branch cut is still crossing the real axis due to over-coupling ($r_2 > r_1$) and the reflection amplitude is forced to be unity due to causality arguments, as verified in Fig.6g)

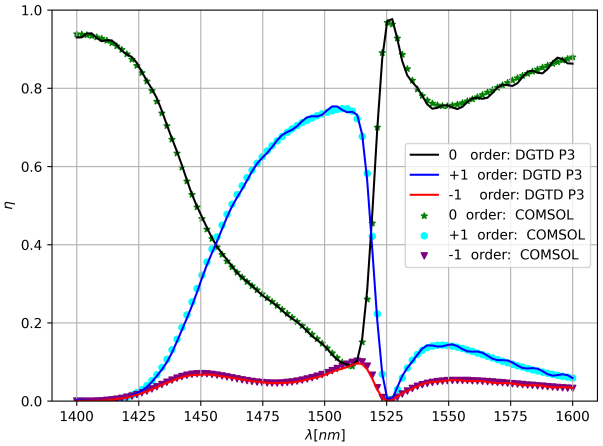

Figure 5 Comparison between results obtained for an active thermal beam steering configuration (see Fig. 3 for more details) using the DG solver developed in our DIOGENeS [71] (lines) and results obtained using the commercial COMSOL Multiphysics® v. 6.0 software (points) based on the FEM methodology. The refractive index distribution have unexpected spatial variation as indicated in the second column of the table. 1.

Additional information for the MQW design

In Fig. 7, we discuss in detail the properties of the unit cell shown in the inset of Fig. 4(a). The response of the unit cell without the lower DBR mirror is shown in Fig. 7(a), where a sharp resonance associated with a π phase around $\lambda = 908$ nm can be observed. The corresponding field profiles are shown in Fig. 7(b), with a strongly localized field distribution within the MQW active region. The evolution of the amplitude and phase as a function of the DBR pairs is shown in Fig. 7(d). In this particular case, 3 DBR pairs are sufficient to achieve 2π phase modulation because the bandwidth of the qBIC mode was chosen to be very small (i.e., close to the real axis), so that any small reflectivity of

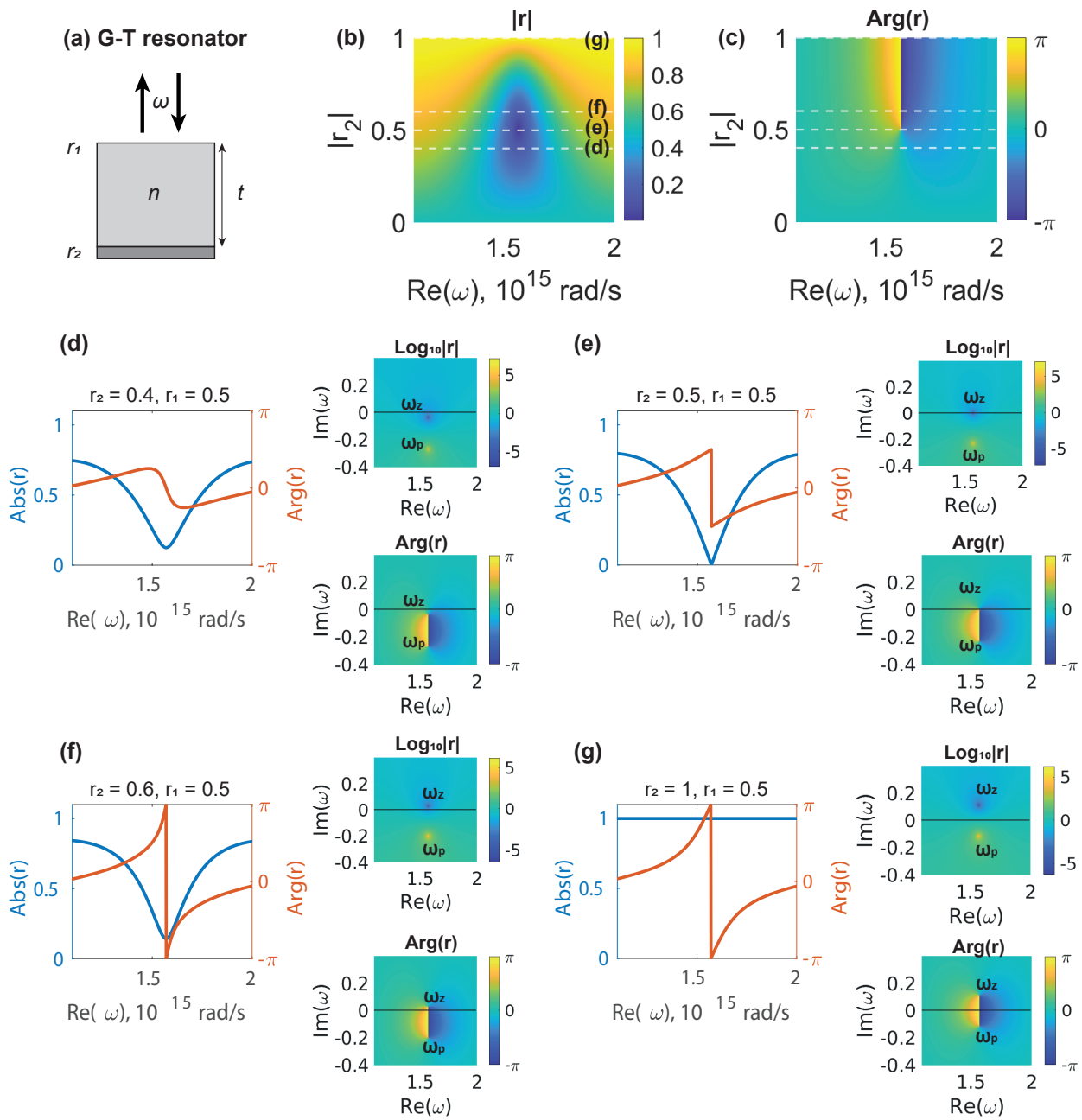

Figure 6 Theoretical analysis of the Gires-Tournois model as a function of the lower mirror reflectivity r_2.(a) Schematic view of the studied G-T model: cavity of refractive index $n = 1.5$ and thickness $t = 600\ nm$ is surrounded with 2 mirrors of reflectivities r_1 and r_2. We assume $r_1 = 0.5$ and study cavity's behaviour for real and complex frequency illumination as a function of r_2. (b) Reflection amplitude and (c) phase maps calculated analytically for G-T cavity varying the bottom mirror reflection r_2 from 0 to 1. (d) $r_2 = 0.4$ As $r_2 < r_1$, both pole and zero are located in a lower part of the complex plane resulting in small phase jump at real frequencies (e) $r_2 = 0.5$ A case of critical coupling. Zero is on a real axis resulting in reflection dip and a π phase jump at real frequency excitation.(f) $r_2 = 0.6$ As $r_2 > r_1$, the zero moves to the upper part of the complex plane, satisfying the condition for which the branch cut connecting zero and pole crosses the real axis. At real frequency excitation, 2π phase accumulation as function of the real frequency appears. (g) $r_2 = 1$ leads to unity reflection in addition to 2π phase jump due to fulfilling $r_2 > r_1$. Unity reflection is accompanied by the condition $\omega_p = \omega_z^*$ in the complex plane.

the lower mirror shifts the reflection zero to the positive real part to achieve 2π phase modulation. However, to achieve the G-T condition with uniform reflection, at least 12 DBR pairs are required (the results for single and 20 DBR pairs are shown in Figs. 7(c-d)). Fig. 8 refers to the performance of the supercell (6 pixels) to achieve efficient beam steering as a function of the binary refractive index distribution n_{QW1} and n_{QW2}. The reflection amplitude in $+1$ mode is shown in Fig. 8(a), an identical response is expected for the -1 mode (data not shown). As it can be seen the optimal beam splitting is achieved with $nQW1 = 3.62$ and $nQW2 = 3.63$ or vice versa. Interestingly, this non-intuitive response cannot be derived from the lookup table in Fig. 4(b) if one applies the corresponding refractive index modulation corresponding to a binary phase of 0 and π. However, near-field coupling plays a crucial role in this highly resonant case, as demonstrated in the lower panel of Fig. 8(b).

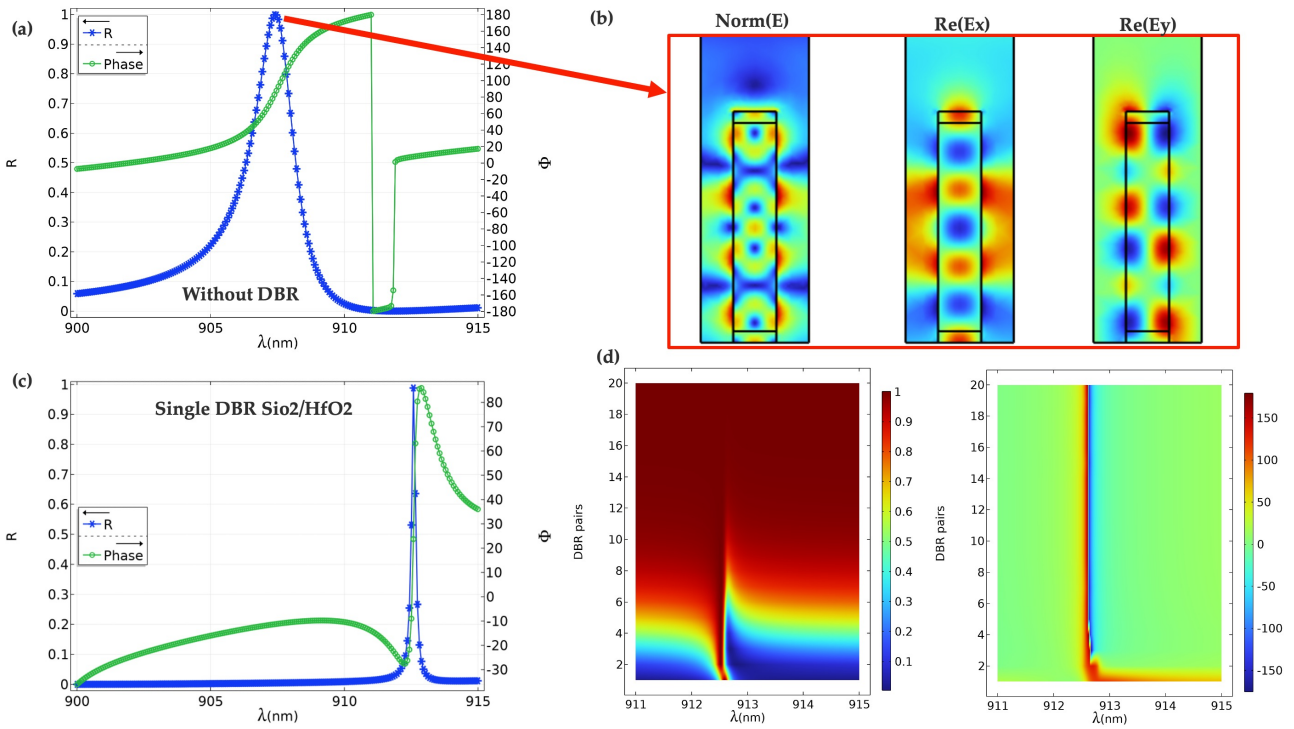

Figure 7 Results of the unit cell for the MQW configuration in Fig. 4. (a) For the amplitude and phase response of the structure without DBR (the single resonator is surrounded by air from above and below). The corresponding field profiles at resonant frequency are given in (b). (c) Amplitude and reflection phase response for a resonator placed on a single DBR pair of Sio_2/HfO_2. (d) for the evolution of amplitude and phase as a function of DBR pairs.

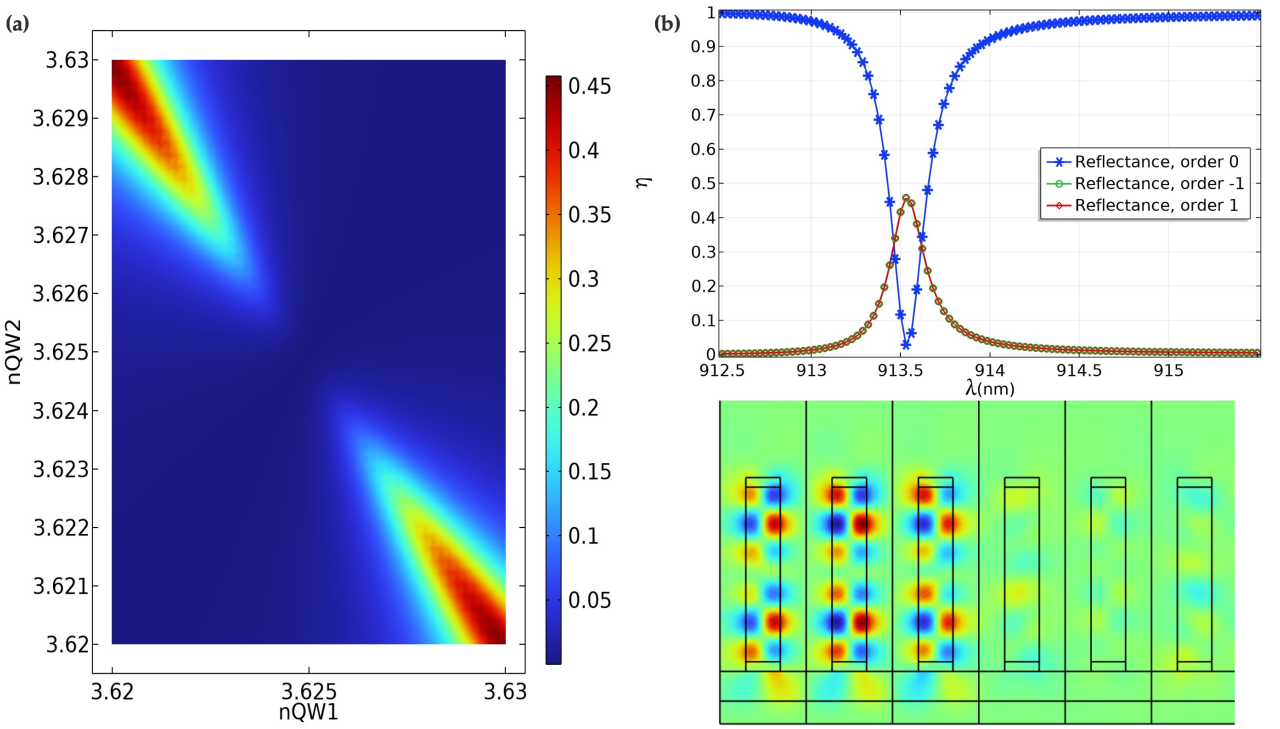

Figure 8 Reflection amplitude of ± 1 mode as a function of a binary refractive index distribution across the first and the second MQW phase tuning elements for a fixed wavelength at $\lambda = 913.5$ nm. The best beam steering performance (90% for both the $+1$ and -1 mode) is obtained when the two values of the refractive index is $nQW1 = 3.62$ and $nQW2 = 3.63$ respectively. (b) Deflection efficiency for as a function of the wavelength. A narrow band-width deflection beam splitting signal reaching 90% efficiency is observed at the optimized wavelength. The time average power flow along x direction is given in the lower panel of (b).